NASA TECHNICAL MEMORANDUM

NASA TM X-850

A COMPARISON OF THE HYPERSONIC STATIC STABILITY CHARACTERISTICS OF BLUNT- AND POINTED-NOSED SLENDER ENTRY VEHICLES

by Barbara J. Short, Ellis E. Whiting,
Robert L. Kruse, and Gerald N. Malcolm
Ames Research Center
Moffett Field, California

NATIONAL AERONAUTICS AND SPACE ADMINISTRATION • WASHINGTON, D. C. • OCTOBER 1963

TECHNICAL MEMORANDUM X-850

A COMPARISON OF THE HYPERSONIC STATIC STABILITY

CHARACTERISTICS OF BLUNT- AND POINTED-NOSED

SLENDER ENTRY VEHICLES

By Barbara J. Short, Ellis E. Whiting,
Robert L. Kruse, and Gerald N. Malcolm

Ames Research Center
Moffett Field, California

NATIONAL AERONAUTICS AND SPACE ADMINISTRATION

NATIONAL AERONAUTICS AND SPACE ADMINISTRATION

_____

TECHNICAL MEMORANDUM X-850

_____

A COMPARISON OF THE HYPERSONIC STATIC STABILITY

CHARACTERISTICS OF BLUNT- AND POINTED-NOSED

SLENDER ENTRY VEHICLES*

By Barbara J. Short, Ellis E. Whiting,
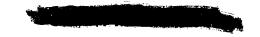Robert L. Kruse, and Gerald N. Malcolm

SUMMARY

The differences in stability between pointed- and blunt-nosed slender entry vehicles at hypersonic speeds have been investigated experimentally and theoretically for two types of configurations - flare-stabilized cylindrical bodies and slender conical bodies. The static stability of these configurations has been measured in the Ames Supersonic Free-Flight Wind Tunnel at Mach numbers of 15 and 17. The data show that the initial stability of both configurations was increased when the blunt nose was replaced with a pointed fairing. The moment curves of the blunt-nosed models of both configurations were highly nonlinear. For the sharp-nosed models with attached flow at low angles of attack, no nonlinearities in the moment curves were observed.

INTRODUCTION

With the change in design of entry vehicles from blunt, low-fineness-ratio bodies to blunt-nosed, slender, flare-stabilized bodies, serious problems which were originally unexpected were encountered in the area of static aerodynamic stability. The stability decreased with increasing Mach number in the hypersonic range, was highly nonlinear, and was badly overestimated by Newtonian theory. These difficulties are noted in references 1 and 2, which also describe a more accurate method for predicting the static stability.

Continuing advances in vehicle design suggest the desirability of using pointed slender bodies for entry vehicles. However, since the static margin decreased when blunt-nosed entry vehicles were made slender, further changes to even more slender shapes would naturally be made with caution. It is necessary, therefore, to study the question both analytically and experimentally to determine whether pointed slender vehicles pose any new aerodynamic stability problems in the hypersonic speed range.

A program to study these questions for two families of slender bodies representative of advanced vehicle design was initiated at the Supersonic Free-Flight Branch of the Ames Research Center, NASA. Objectives were (1) to determine theoretically and experimentally the static stability of a pointed flare-stabilized configuration at a Mach number of 15 for comparison with the stability of this same body with a blunt nose, and (2) to obtain and compare with theory the effect on the static stability of a slender cone of various amounts of spherical and ogival bluntness.

SYMBOLS

A reference area, based on d, sq ft

C_D drag coefficient, based on A, dimensionless

C_{D_i} initial (at $\alpha = 0$) drag coefficient, dimensionless

C_m pitching-moment coefficient, based on A and s, dimensionless

C_{m_α} pitching-moment-curve slope, per radian

$C_{m_{\alpha_i}}$ initial (at $\alpha = 0$) pitching-moment-curve slope, per radian

C_{N_α} normal-force-curve slope, per radian

d flared-model cylinder diameter or conical-model base diameter, ft

I moment of inertia about a transverse axis through the center of gravity, slug-ft^2

l model length, ft

M Mach number, dimensionless

m mass of model, slugs

p static pressure, lb/sq ft

p_∞ free-stream air static pressure, lb/sq ft

q dynamic pressure, lb/sq ft

q_∞ free-stream air dynamic pressure, lb/sq ft

r radial distance measured from model axis, ft

r_b base radius, ft

r_N nose radius of curvature, ft

R Reynolds number based on free-stream conditions and d, dimensionless

s reference dimension, length of blunt-nosed flared models or base diameter of conical models, ft

V model velocity relative to air stream, ft/sec

x distance from nose along model axis, ft

x_{cg} distance from nose to center-of-gravity location, ft

x_{cp} distance from nose to center-of-pressure location, ft

α angle of attack, deg

α_{rms} root-mean-square angle of attack, deg

Γ stability parameter, $\dfrac{1}{\lambda^2}\dfrac{I}{\rho As}$, dimensionless

Γ_i initial (at $\alpha = 0$) stability parameter, dimensionless

θ_N nose-tangent angle, deg

λ wave length of oscillation, ft/cycle

ν Prandtl-Meyer angle, deg

ρ free-stream air density, slugs/cu ft

σ_m maximum resultant angle of pitching oscillation, deg (see sketch (a))

σ_0 minimum resultant angle of pitching oscillation, deg (see sketch (a))

MODELS AND TEST CONDITIONS

A sketch of the models tested is shown in figure 1. Figure 1(a) shows superimposed the pointed-nosed, flare-stabilized configuration tested in the present investigation and the spherical-nosed configuration tested in a prior program. The models were constructed from two materials, a tungsten alloy and aluminum, so that the center of gravity could be positioned at the indicated distance from the base for both models. Figure 1(b) shows the 12.5° half-angle cone with a series of tangent ogives with nose angles of 90° (spherical), 45°, 20°, and 12.5° (the sharp cone). These models were also bimetallic in construction. To determine the center-of-pressure location of the conical models each configuration was tested with two center-of-gravity locations. The center of gravity was positioned about 0.74d and 0.84d from the base, except for the sharp cone

where it was about 0.90d and 1.02d from the base. These locations, along with other model measurements, test conditions, and final results, are listed in table I.

The models were launched from a single-stage, shock-heated, light-gas gun into a Mach number 3 countercurrent air stream. The combined velocity of the model and air stream was approximately 10,000 ft/sec for the flared models and 12,000 ft/sec for the conical models, corresponding to Mach numbers of about 15 and 17, respectively. The time-distance histories and the attitude histories of the models in free flight were recorded by nine spark-shadowgraph stations along the flight path.

METHOD OF ANALYSIS

Theoretical Procedures

The static aerodynamic stability of the flare-stabilized configuration was analyzed theoretically by separate consideration of the three component parts - the nose, the cylinder, and the flare. The contribution of the nose segment to normal force and pitching moment was determined by modified Newtonian impact theory. The contribution of the cylinder was found by the method discussed in references 1 and 2, hereinafter referred to as the $\Delta v = \alpha$ method. The flare contribution to stability was determined by embedded Newtonian flow theory, an impact flow theory with the stream properties approaching the ramp as initial conditions, as described in references 1 and 3. The above procedures resulted in stability coefficients for each segment which were combined for the total stability of the vehicle.

In order to use the theoretical procedures outlined in the previous paragraph it is necessary to know the static pressure distribution along the cylinder and the dynamic pressure distribution over the flare at zero angle of attack. These properties for a real gas in equilibrium flow can be computed by the numerical procedure described in reference 4. This method of flow-field construction is based on a known bow-shock-wave profile and assumes a radial pressure distribution mathematically similar to the blast-wave pressure distribution between the body surface and the shock wave. To estimate the static stability, therefore, it was necessary to construct an approximate bow shock wave.

The estimated shock wave for the pointed flare-stabilized body was constructed in the following way: The computed conical shock wave over the nose was extended to the first point of interaction between the shock wave and the expansion fan emanating from the cone-cylinder junction. Far downstream the form of the wave was assumed to be $r/d = K(x/d)^{1/2}$, as specified by blast-wave theory. The coefficient, K, was taken to be 0.65 from an extrapolation of the shock-wave data in figure 14 of reference 5. In logarithmic coordinates these two shock-wave segments appear as intersecting straight lines. In order to make the shock-wave slope continuous at all points, a transition section, described analytically by a circular arc in the $\log(r/d)$, $\log(x/d)$ plane, joined the nose-region segment and the downstream segment. After the tests, the actual shock wave was

measured and another estimate of static stability was computed based on the true shock wave. The constructed shock wave is compared with the experimental shock wave in figure 2.

The zero angle-of-attack pressure distributions over the cylinder, computed by the procedure outlined in reference 4, are shown in figure 3. Also shown in this figure is the pressure distribution for the blunt-nosed body, which was calculated from an experimental shock wave during the previous program. Although the pressure distribution for the pointed body is unusual in that it shows a station of maximum surface pressure about one diameter behind the cone base, it does fair in smoothly with the pressure just downstream of the nose-cylinder junction found by expanding the cone flow (ref. 6) onto the cylinder, and, further, it comes into agreement with the pressure for the blunt-nosed body farther downstream where the effects of detailed differences in nose shape have diminished.
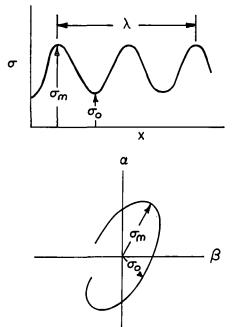
The computed dynamic-pressure distributions incident on the flare at zero angle of attack for both the blunt- and pointed-nosed bodies are shown in figure 4. The much higher dynamic-pressure ratio over the flare surface for the pointed body is immediately apparent. With the dynamic pressure higher by this amount, the normal force on the flare of the pointed body will be approximately 2-1/2 times that for the blunt-nosed body according to references 1 and 3.

Figure 5 shows the computed distribution of the incremental normal-force-curve slope along the model axis for both the pointed- and blunt-nosed bodies. The normal force of the pointed body is appreciably higher than that of the blunt body and is distributed in a way to give a more rearward position of the center of pressure. The static stability of the pointed body about the center of gravity shown in figure 1(a) is computed to be about three times that of the blunt body.

The simpler shapes of the series of conical configurations lend themselves to less complicated theoretical analysis. The theoretical results for these models were obtained by use of modified Newtonian impact theory, the $\Delta v = \alpha$ method, and, for the sharp cone, conical flow theory (ref. 6). The values of $C_{m\alpha_i}$ computed by impact theory were more than twice those computed by the $\Delta v = \alpha$ method for all the cones.

Data Reduction

The method of data presentation used in this report follows the development presented in reference 7 and further discussed in reference 8. In this method the static stability is deduced from the measured wave length of oscillation, λ, (see sketch (a)) by means of the following relation, $\Gamma = (1/\lambda^2)(I/\rho As)$.

Sketch (a)

It has been shown in reference 8 that Γ is a convenient parameter which describes the stability of a vehicle in free flight. This method of data presentation permits analysis of nonlinear pitching moments when Γ is plotted versus the amplitude of oscillation in the form $(\sigma_o^2 + \sigma_m^2)$. For complex nonlinear cases, the methods of references 9, 10, and 11 can be applied, under suitable restrictions, to define the pitching-moment curve.

In this report, whenever a complex nonlinear case was indicated, the method of reference 11, as discussed in the appendix of reference 8, was used. This method was developed on the assumption of planar pitching motion and for very nearly sinusoidal oscillations. Although the present tests did not display truly planar pitching motion, they did fall within the empirically defined limits of planar motion given in reference 10 as reasonably planar motion with $\sigma_o/\sigma_m \leq 1/3$. The analysis of reference 11 is approximate, but can, nevertheless, be applied to cases in which the pitching moment is represented to any degree in odd powers of α. Furthermore, the solution is easy to apply and has been found to give reliable answers.
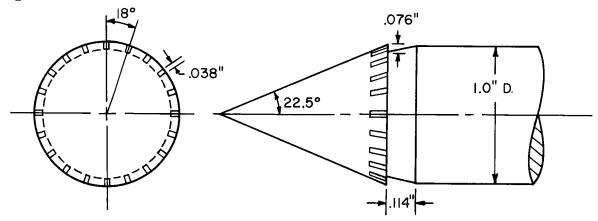

RESULTS AND DISCUSSION

Flare-Stabilized Models

The experimental data for these models in terms of Γ vs. $(\sigma_o^2 + \sigma_m^2)$ are shown in figure 6. The reference dimension used to calculate Γ was the length of the blunt-nosed model. The blunt-body data are reproduced from reference 2. The data for the pointed body lie above the blunt-body data, particularly at small angles of attack. However, considerable scatter is apparent in the pointed-body data, especially in the case of the smallest pitching amplitude run, run 976. The first pointed-body test (run 965 in table I) was made at a free-stream Reynolds number of 1.34 million, based on cylinder diameter. An examination of the shadowgraph record for this test indicated the boundary layer was laminar and the flow separated over most of the cylinder, even near zero angle of attack. It has been shown in reference 12 that a separated boundary layer increases the stabilizing effect of the flare. However, an evaluation of the theoretical methods described above and a valid comparison with the blunt-nosed body could be made only for attached flow. An effort was, therefore, made to eliminate the separation by increasing the free-stream Reynolds number for all subsequent tests to the maximum attainable at this model scale and velocity, approximately 2.3 million based on body diameter. This increase in Reynolds number reduced the amount of separation at zero angle of attack, but did not noticeably alter the separation pattern at angles of attack above 3° or 4°.

Because increasing the Reynolds number did not eliminate flow separation, an additional step was taken. It is well known that a turbulent boundary layer is more difficult to separate than a laminar one. Therefore, the models were modified to initiate turbulence in the boundary layer at the cone-cylinder junction. Sketch (b) shows the boundary-layer trip used to promote turbulence. It was considered that vorticies formed by the flow passing through the slots on the nose should tend to trip the boundary layer. Although the modification to the

cylindrical portion of the model probably had a slight destabilizing effect on over-all missile stability, the amount was estimated to be small and, hence, was disregarded.

Sketch (b)

Two modified models were tested and the data are shown by the filled symbols in figure 6. The shadowgraph records indicate that the boundary layer on these test models was indeed turbulent. Also the record shows that boundary-layer separation did not occur on the low amplitude test ($\sigma_m = 3.1°$) but did occur on the high angle-of-attack test ($\sigma_m = 11.5°$) at angles of attack of 7° and greater. The low amplitude test provides a good measure of the initial ($\sigma = 0$) stability with attached flow.

The theoretical estimates of Γ_i are also shown in figure 6. The estimate of Γ_i, computed from the experimental shock-wave shape, is about 25 percent lower than the indicated value of Γ_i for the attached-flow experimental data. It was found in reference 2 that the theory also underestimated the stability of the blunt-nosed configuration, as indicated in figure 6.

The pitching-moment curves corresponding to the experimental data and theoretical estimates shown in figure 6 are presented in figure 7. A comparison of the stability of blunt- and pointed-nosed bodies with attached flow is shown in figure 7(a). The blunt-body data and analyses are from reference 2, as noted earlier. If the flow is attached at low angles of attack, the effect of the pointed nose is to increase the stability and eliminate the nonlinearity of the pitching-moment curve. However, the boundary layer is more likely to separate if the nose is pointed. The effect of separation on the stability of the pointed-nosed body is shown in figure 7(b). Boundary-layer separation in this case has two effects on the static stability: (1) in the low amplitude region the stability is markedly increased, and (2) the pitching moment becomes a highly non-linear function of angle of attack.

Conical Models

The experimental measurements for the series of conical models are summarized in table I(b). Figure 8 shows the results for the sphere cone with

both locations of the center of gravity. The stability parameter, Γ, is plotted against $(\sigma_0^2 + \sigma_m^2)$ in figure 8(a). The curve for the models with the forward center of gravity is in doubt at values of $(\sigma_0^2 + \sigma_m^2)$ less than 150 because of the lack of data at small angles of attack. Therefore, two fairings are shown; they will be discussed later.

Included in the figure are the values of Γ at zero angle of attack calculated by the $\Delta v = \alpha$ method and by modified Newtonian impact theory. The initial stability calculated by the $\Delta v = \alpha$ method agrees within 20 percent with the experimental data; whereas, the impact theory predicts an initial stability 2.5 times greater than measured.

The pitching-moment curves deduced from these experimental data are shown in figure 8(b) along with the curves calculated by use of Newtonian theory and the initial slopes calculated by the $\Delta v = \alpha$ method. At low angles of attack, the pitching moment agrees with that predicted by the $\Delta v = \alpha$ method; however, the pitching-moment curve is highly nonlinear and agrees with Newtonian theory at angles of attack greater than the half-angle of the cone.

The center-of-pressure location calculated from the pitching-moment curves for the two center-of-gravity locations is shown in figure 8(c). The solid curve was obtained with the use of the solid curves in figure 8(a). The effect of moving the upper curve in figure 8(a) to the position indicated by the dashed curve is shown by the dashed curve in figure 8(c). This uncertainty in the center-of-pressure position at low angles of attack, a consequence of the lack of data in this region for the models with the forward center of gravity, has little effect on the pitching-moment curve (fig. 8(b)).

The data for the 45° ogive cone, the 20° ogive cone, and the sharp cone showed no variation of the stability parameter with $(\sigma_0^2 + \sigma_m^2)$ to values of about 300. Therefore, the pitching-moment-curve slope, $C_{m\alpha}$, is constant for a given center of gravity and was plotted versus center-of-gravity location (fig. 9) to determine the normal-force-curve slope and the center-of-pressure location (fig. 10). These data are shown along with the curves calculated by use of modified Newtonian impact theory, the $\Delta v = \alpha$ method, and conical-flow theory. The previously discussed center-of-pressure location for the sphere-cone configuration at $\alpha = 0$, and the corresponding normal-force-curve slope, $C_{N\alpha}$, are included in figure 10. The nose-tangent angle is used as the independent variable for clarity in presenting the data. As can be seen in figure 1(b), these configurations form a family of shapes with varying nose radius of curvature from infinity for the sharp cone to 0.25d for the sphere cone. The symbols in figure 10 are the results of fairing best fitting lines to the data of figure 9. The symbols are barred to show the possible extreme limits of the values as a result of the scatter in the data of figure 9. Figure 10(a) shows that $C_{N\alpha}$ is not well defined by the data but is generally smaller than predicted, except for the sphere-cone and the 45° ogive-cone configurations where the results of the $\Delta v = \alpha$ method agree with the experimental results. Figure 10(b) shows the center of pressure of the sharp cone and the ogive cones to be farther aft than predicted. The center of pressure of the sphere cone at zero angle of attack is between the locations predicted by Newtonian theory and the $\Delta v = \alpha$ method.

Figures 9 and 10 indicate that the $\Delta v = \alpha$ method is not reliable for the bodies with pointed tips whereas the modified Newtonian theory is reasonably accurate for such shapes.[1]

If we consider the nose radius of the spherically tipped cone as being progressively reduced toward zero, then another method of transition between the present blunt-nosed and pure cone configurations is described. To investigate the relationship of experiment to theory in such a case, the slightly blunted cone shown in figure 11 ($r_N/d = 0.062$) was tested with one center-of-gravity location. Figure 11(a) shows the stability parameter along with initial values of Γ calculated by the $\Delta v = \alpha$ method and by use of modified Newtonian impact theory. The data show a higher initial stability than predicted by either method. Figure 11(b) shows the pitching-moment curve along with the curve calculated by use of modified Newtonian theory and the initial slope calculated by the $\Delta v = \alpha$ method. Modified Newtonian theory underestimates the pitching-moment coefficient by about 30 percent at the low angles of attack and about 10 percent at angles of attack greater than the cone half-angle. The initial slope predicted by the $\Delta v = \alpha$ method is about one-third of the experimental value.

To show the effect of bluntness on stability for the family of spherical-tipped 12.5° cones, the initial pitching-moment-curve slopes for a center-of-gravity location of 0.89 diameter forward from the base are plotted versus the ratio of nose-to-base radius in figure 12. The value of $C_{m_{\alpha_i}}$ for the 50-percent blunt sphere cone at this shifted center-of-gravity location was calculated from the experimental normal-force-curve slope and center-of-pressure location. The data indicate that there is an optimum bluntness for maximum stability between the sharp cone and the 50-percent blunt sphere cone. Included in figure 12 are the curves obtained by the $\Delta v = \alpha$ method and modified Newtonian impact theory as well as the value predicted by conical flow theory. It can be seen that conical flow theory predicts the stability of the sharp cone very satisfactorily for this center of gravity. Newtonian theory predicts increasing stability with increasing bluntness and becomes inaccurate for this class of bodies as the bluntness is increased. The $\Delta v = \alpha$ method is inaccurate for pointed and slightly blunted cones and appears to be useful only for blunt-nosed slender bodies whose length is limited to a few nose diameters.

It is interesting to note that for both the flare-stabilized and the conical configurations, the pitching-moment curve is highly nonlinear for the models with blunt noses, and the nonlinearity decreases with decreasing nose bluntness. Also, for both configurations, the initial stability is increased when the blunt nose is replaced with a weightless pointed fairing.

Drag coefficients were also obtained for all of the conical models tested, and the results are summarized in figure 13. In figure 13(a), C_D is shown as a function of the mean-squared angle of attack. Within the scatter of the data, the drag is the same for the sharp cone, the 20° ogive cone, and the 12.5-percent blunt sphere cone.

---

[1]Little theoretical justification can be found for applying the $\Delta v = \alpha$ method to pointed-nosed bodies. In the case of spherical-nosed bodies, however, theoretical reasons exist why the method should be valid to a distance of a few nose diameters behind the blunt nose.

Cross plots of the drag coefficients at zero angle of attack, C_{D_i}, are shown in figures 13(b) and (c) along with the wave-drag coefficients predicted by modified Newtonian impact theory and conical flow theory. The measured total drag of the 50-percent blunt sphere cone and the 45° ogive cone agrees with the values of wave drag predicted by impact theory. The sizable disagreement between the experimental and theoretical values for the more pointed models is somewhat surprising. For the sharp cone, the measured total drag is about 37 percent higher than predicted by conical flow theory. Estimates show that skin friction and base drag could account for a maximum of about 15 percent of this difference. The shock-wave angle measured from the shadowgraphs agrees with the value predicted by conical flow theory. The test conditions were not in the region where viscous interaction effects are important (according to existing theory) and the maximum possible induced pressure drag could account for only 2 percent of the difference.

Another possible explanation for the high measured drag of the pointed models is the possibility of model damage. The models were bimetallic and underwent high acceleration loads during launch. The bow shock wave was so close to the body that the shadowgraphs could not reveal disturbances which would result from deformations in the model. Estimates show that the stress at the joint for the sharp cone and the 12.5-percent blunt cone could have been equal to the compressive strength. However, for the 20° ogive cone the stress at the joint could not have been over 55 percent of the compressive strength and these models exhibited the same high drag as the sharp cone. This would suggest that model damage is not the cause of the discrepancy.

CONCLUSIONS

The effect of nose shape on the static stability of slender entry vehicles at hypersonic speed has been investigated for flare-stabilized configurations and for a series of conical configurations. On the basis of the results presented herein, the following conclusions can be drawn.

1. For both the flare-stabilized bodies and the slender conical bodies, the initial stability is increased when the blunt nose is replaced with a weightless pointed fairing.

2. The pitching-moment curves are highly nonlinear for the blunt-nosed bodies, and the nonlinearities decrease with decreasing nose bluntness.

3. For the flare-stabilized bodies, predictions by the method of reference 1 indicate the correct trend of change in initial stability with nose bluntness.

4. On flare-stabilized vehicles, the boundary layer is more likely to separate if the nose is sharp. If separation occurs, the stability increases markedly and the pitching-moment curve becomes highly nonlinear.

5. For spherically tipped cones, the maximum initial stability occurs with an intermediate bluntness between the sharp cone and the 50-percent blunt sphere cone; whereas, modified Newtonian impact theory predicts (incorrectly) a uniform trend of increasing stability with increasing bluntness. The $\Delta v = \alpha$ method apparently should be restricted to blunt-nosed bodies whose length is limited to a few nose diameters.

Ames Research Center
    National Aeronautics and Space Administration
        Moffett Field, Calif., June 25, 1963

REFERENCES

1. Seiff, Alvin, and Whiting, Ellis: The Effect of the Bow Shock Wave on the Stability of Blunt-Nosed Slender Bodies. NASA TM X-377, 1960.

2. Whiting, Ellis E., and Carros, Robert J.: Free-Flight Investigation of the Static Stability and Aerodynamic Drag of Three Blunt-Nosed Cylinder-Flare Test Bodies at Mach Numbers From 13 to 17. NASA TM X-500, 1961.

3. Seiff, Alvin: Secondary Flow Fields Embedded in Hypersonic Shock Layers. NASA TN D-1304, 1962.

4. Seiff, Alvin, and Whiting, Ellis E.: Calculation of Flow Fields From Bow-Wave Profiles for the Downstream Region of Blunt-Nosed Circular Cylinders in Axial Hypersonic Flight. NASA TN D-1147, 1961.

5. Seiff, Alvin, and Whiting, Ellis E.: A Correlation Study of the Bow-Wave Profiles of Blunt Bodies. NASA TN D-1148, 1962.

6. Staff of the Computing Section, under the direction of Zdenek Kopal, Massachusetts Inst. of Tech., Dept. of Elect. Engr., Center of Analysis: Tables of Supersonic Flow Around Yawing Cones. Tech. Rep. No. 3, Cambridge, 1947.

7. Rasmussen, Maurice L.: Determination of Nonlinear Pitching-Moment Characteristics of Axially Symmetric Models From Free-Flight Data. NASA TN D-144, 1960.

8. Whiting, Ellis E.: An Exploratory Investigation of Fins as Stabilizers for Blunt-Nosed Slender Bodies at Hypersonic Speeds. NASA TM X-657, 1962.

9. Murphy, Charles H.: The Measurement of Nonlinear Forces and Moments by Means of Free-Flight Tests. BRL Rep. 974, Aberdeen Proving Ground, 1956.

10. Kirk, Donn B.: A Method for Obtaining the Nonlinear Aerodynamic Stability Characteristics of Bodies of Revolution From Free-Flight Tests. NASA TN D-780, 1961.

11. Kryloff, N., and Bogoliuboff, N. (Solomon Lefschetz, trans.): Introduction to Non-linear Mechanics. Annals of Mathematics Studies. No. 11. Princeton Univ. Press, 1943.

12. Dennis, David H.: The Effects of Boundary-Layer Separation Over Bodies of Revolution With Conical Tail Flares. NACA RM A57I30, 1957.

TABLE I.- TEST CONDITIONS, MODEL MEASUREMENTS, AND TEST RESULTS

(a) Flare-stabilized models

Run no.	M	$R \times 10^{-6}$ based on d	V, ft/sec	$\rho \times 10^3$, slugs/ft^3	$m \times 10^3$, slug	$I \times 10^7$, slug-ft^2	λ, ft/cycle	σ_o, deg	σ_m, deg
Blunt nosed									
448	16.0	1.38	10730	0.902	0.366	2.340	50.8	1.3	5.4
450	14.4	1.25	9670	.906	.366	2.350	29.5	1.0	18.4
546	14.9	2.12	10220	1.515	.368	2.350	27.7	1.3	13.9
Sharp nosed									
965	14.8	1.34	9860	.939	.335	2.790	32.2	.5	4.8
975	15.2	2.33	10190	1.595	.328	2.690	27.8	.7	6.3
976	15.2	2.32	10140	1.593	.330	2.740	28.0	.7	1.5
1037	14.3	2.07	9700	1.538	.323	2.631	28.7	.3	8.5
1038	14.1	2.13	9560	1.596	.329	2.761	30.3	0	11.5
1042	15.0	2.18	10150	1.543	.327	2.720	30.8	1.4	9.8
1045	15.0	2.18	10190	1.530	.328	2.721	25.0	1.0	4.7
1047	14.9	2.18	10080	1.553	.322	2.665	23.6	.7	2.3
1055	14.7	2.22	9990	1.572	.313	2.606	31.3	.2	11.5
1056	14.6	2.14	9950	1.528	.312	2.601	30.8	.6	3.1

(b)   Conical models

Run no.	M	$R \times 10^{-6}$ based on d	V, ft/sec	$\rho \times 10^3$, slugs/ft^3	$m \times 10^3$, slug	$I \times 10^7$, slug-ft^2	λ, ft/cycle	σ_o, deg	σ_m, deg
Sphere cone, $x_{cg}/d = 0.613$
929	17.1	2.59	11610	0.922	0.361	0.807	23.3	3.9	16.6
931	13.0	2.65	12320	.899	.358	.792	29.8	1.1	6.5
934	17.3	2.57	11880	.907	.358	.796	28.9	.2	6.9
947	17.5	2.75	11790	.942	.357	.810	25.5	.3	9.5
948	17.6	2.80	11800	.955	.357	.814	22.7	3.3	16.3
961	17.2	2.68	11520	.929	.364	.825	27.2	.3	8.9
989	17.4	2.79	11680	.952	.355	.789	33.5	.7	3.5
990	17.8	2.74	12010	.919	.353	.790	27.7	1.1	8.2
1012	16.7	2.63	11180	.946	.354	.807	23.3	2.6	13.5
1015	17.7	2.83	11840	.957	.358	.817	25.7	.3	10.1
1032	17.6	2.69	11950	.927	.359	.821	23.6	1.5	13.4
1064	16.0	2.18	11180	.851	.352	.761	23.8	6	120
Sphere cone, $x_{cg}/d = 0.522$
1013	15.9	2.48	10700	.945	.312	.503	15.4	.6	18.3
1014	16.6	2.60	11220	.942	.291	.484	16.6	.3	12.9
1018	16.4	2.52	11110	.929	.292	.505	15.7	.2	17.5
1024	15.9	2.44	10840	.931	.304	.504	15.4	.4	21.3
1051	15.7	2.45	10670	.948	.320	.520	17.2	.1	12.5
45° tangent ogive cone, $x_{cg}/d = 0.849$
932	17.2	4.39	11530	1.539	.275	.856	19.3	1.5	17.6
936	17.9	2.76	12080	.932	.283	.900	26.1	.3	8.6
938	18.0	2.76	12240	.936	.272	.874	25.2	.7	15.6
940	18.2	2.83	12340	.942	.272	.874	25.7	2.3	11.2
45° tangent ogive cone, $x_{cg}/d = 0.742$
1023	17.2	2.67	11570	.939	.217	.590	17.8	.8	12.9
1027	16.7	2.47	11420	.908	.226	.595	18.2	.6	10.7
1029	16.7	2.52	11350	.924	.232	.604	16.9	.2	13.3
1057	16.2	2.32	11290	.886	.239	.616	18.4	1.0	11.1
1058	16.4	2.40	11330	.911	.239	.616	18.3	.6	12.7

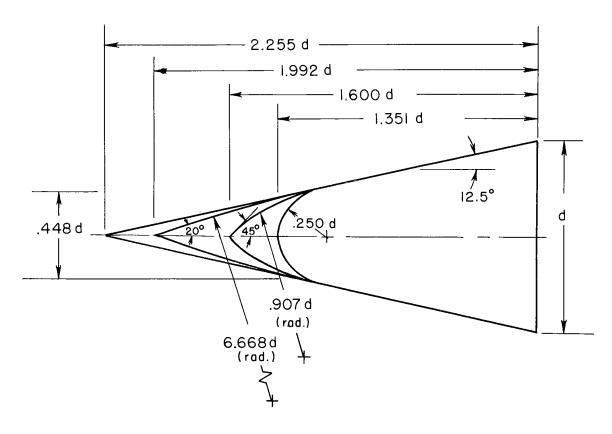TABLE I.- TEST CONDITIONS, MODEL MEASUREMENTS, AND TEST RESULTS - Concluded

(b)   Conical models - Concluded

Run no.	M	$R \times 10^{-6}$ based on d	V, ft/sec	$\rho \times 10^3$, slugs/ft^3	$m \times 10^3$, slug	$I \times 10^7$, slug-ft^2	λ, ft/cycle	σ_0, deg	σ_m, deg
20° tangent ogive cone, $x_{cg}/d = 1.282$									
1033	17.5	2.64	11780	0.907	0.221	0.884	31±1	1.5±.5	8.5±.5
1034	17.8	2.68	12160	.918	.222	.879	32.2	.6	5.0
20° tangent ogive cone, $x_{cg}/d = 1.144$									
1016	17.3	2.70	11650	.939	.295	1.175	24.5	2.2	13.0
1019	16.4	2.52	11120	.926	.292	1.181	25.0	.8	9.3
1030	17.2	2.60	11740	.918	.293	1.174	24.0	2.1	5.6
Sharp cone, $x_{cg}/d = 1.360$									
939	17.2	2.62	11710	.925	.300	1.378	25.6	1.4	11.6
958	17.8	2.71	12020	.925	.296	1.335	25.2	1.7	7.6
959	17.5	2.62	11870	.913	.297	1.360	25.9	.5	7.3
988	17.9	2.77	12070	.934	.300	1.334	24.8	.6	13.8
991	17.8	2.77	12020	.935	.301	1.382	25.2	1.5	9.2
994	17.6	2.82	11810	.952	.301	1.356	24.7	1.2	6.4
1050	16.9	2.55	11490	.918	.299	1.367	25.4	.2	7.8
Sharp cone, $x_{cg}/d = 1.230$									
1022	16.2	2.52	10920	.939	.254	.875	16.8	6.4	13.0
1025	16.5	2.48	11280	.917	.269	.913	18.0	3.6	15.5
1028	16.8	2.64	11310	.949	.262	.913	17.6	.3	17.0
1053	16.7	2.52	11420	.919	.262	.940	18.0	1.0	11.3
1054	16.4	2.50	11150	.926	.259	.940	18.3	.4	10.3
12.5-percent blunt sphere cone, $x_{cg}/d = 1.142$									
983	17.9	2.83	12050	.944	.300	1.371	22.2	1.1	6.1
1060	16.9	2.43	11760	.891	.294	1.305	22.7	1.3	6.6
1061	17.2	2.62	11660	.926	.292	1.260	24.6	1.4	19.4
1063	17.7	2.42	12390	.851	.295	1.305	24.8	1.1	13.2

16

(a) Flare-stabilized models, d = 0.258 inch.

(b) Conical models, d = 0.450 inch.

Figure 1.- Sketches of models.
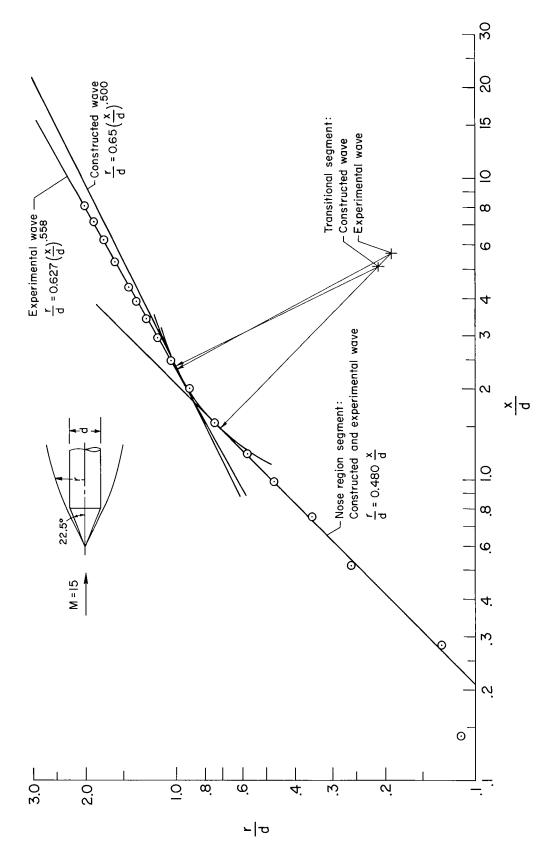
Figure 2.- Comparison of constructed and experimental shock waves for cone-cylinder-flare model.
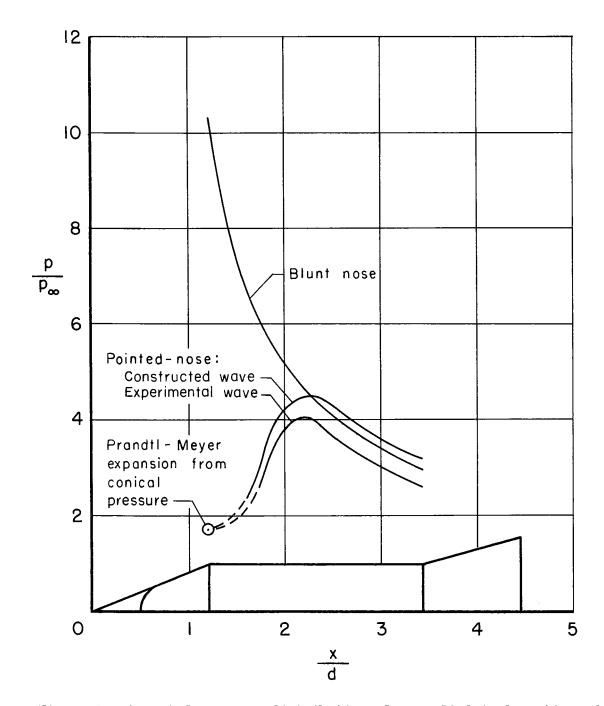
Figure 3.- Computed pressure distribution along cylindrical section of flare-stabilized bodies by method of reference 4; M = 15.
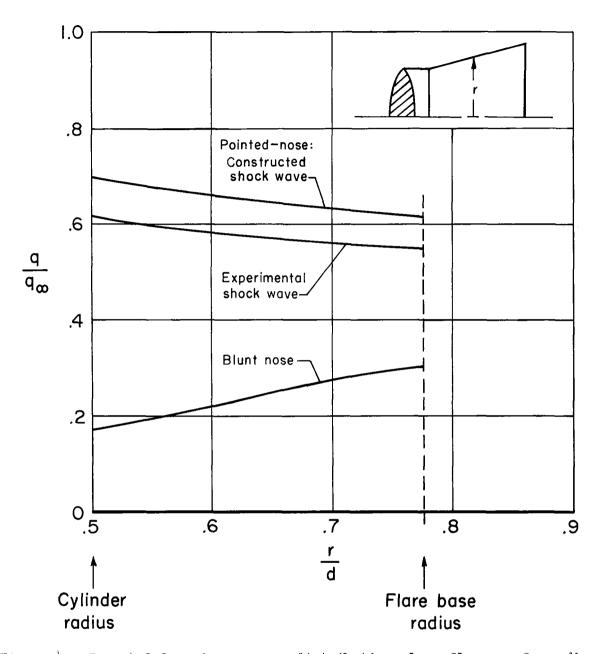
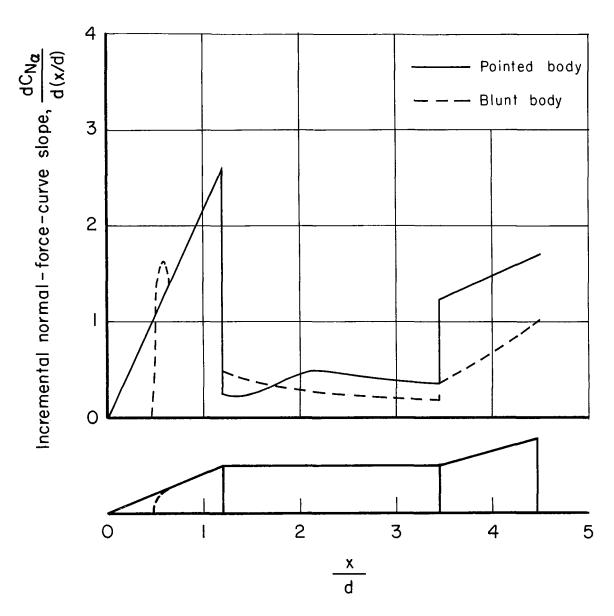Figure 4.- Computed dynamic-pressure distribution along flare surface; M = 15.
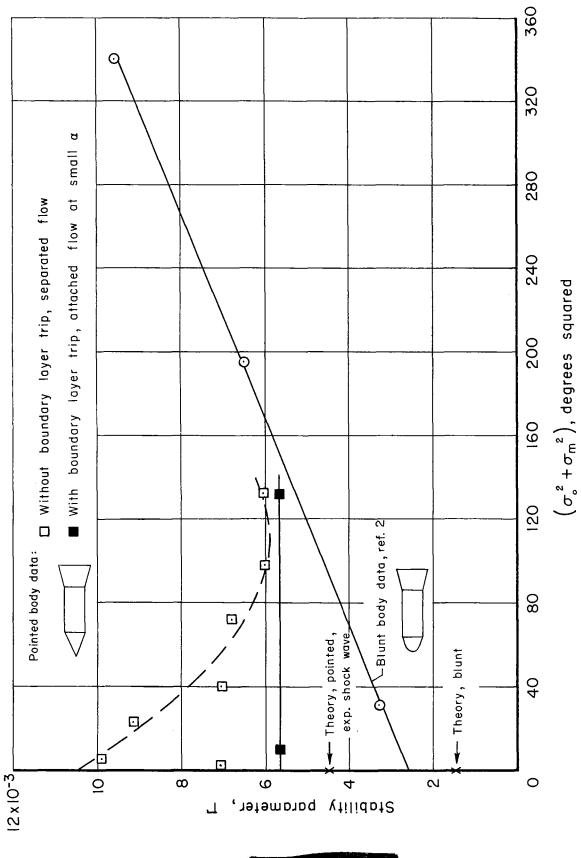
Figure 5.- Distribution of computed incremental normal-force-curve slope.

Figure 6.- Stability data of flare-stabilized bodies; M = 15.

(a) Comparison of blunt- and pointed-nosed bodies with attached flow at low angles of attack.
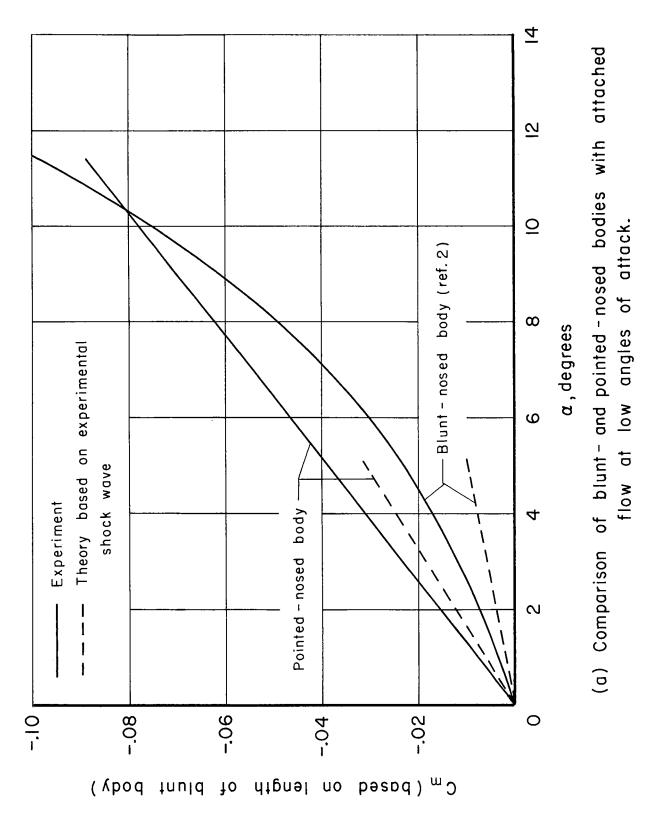
Figure 7.- Pitching-moment coefficient for flare-stabilized configuration; M = 15.

(b) Comparison of separated and attached flow on pointed-nosed body.

Figure 7.- Concluded.

(a) Variation of stability parameter with $\left(\sigma_o{}^2 + \sigma_m{}^2\right)$.
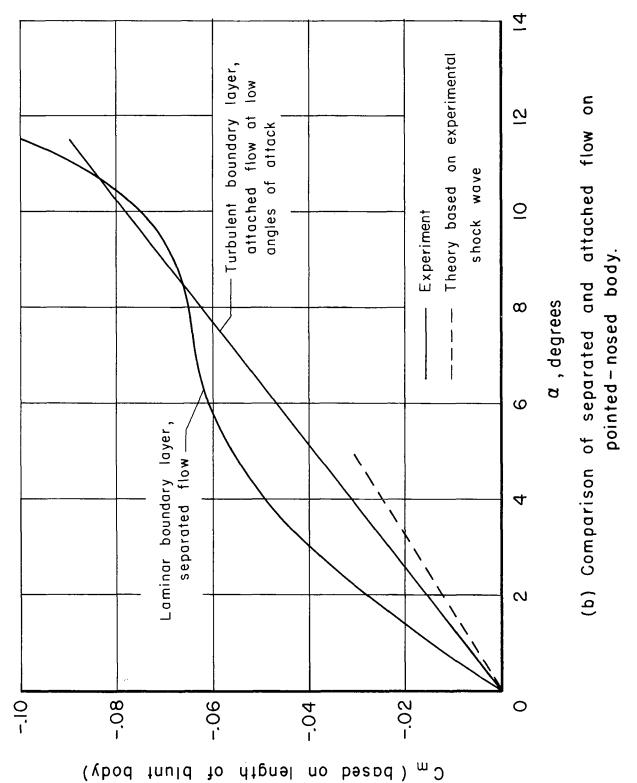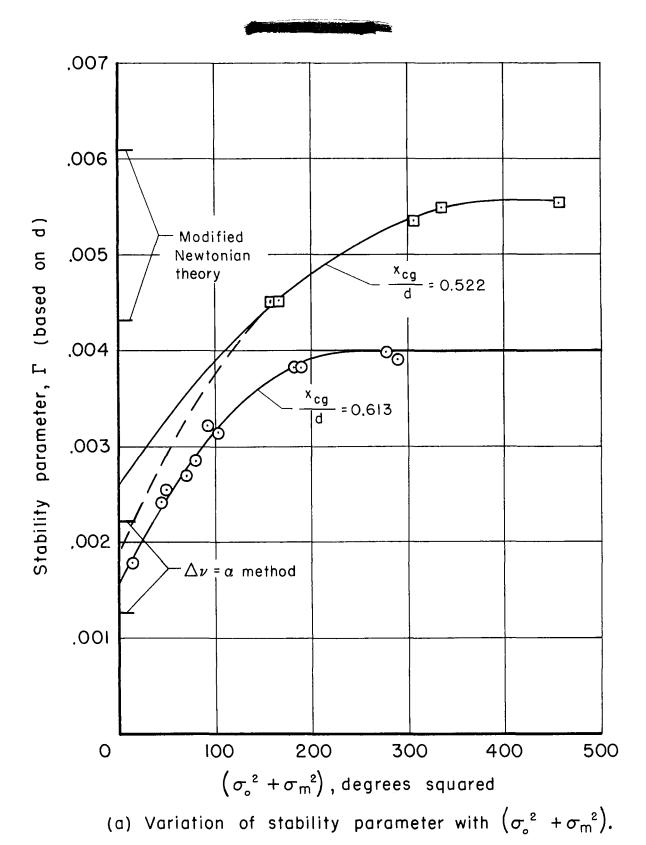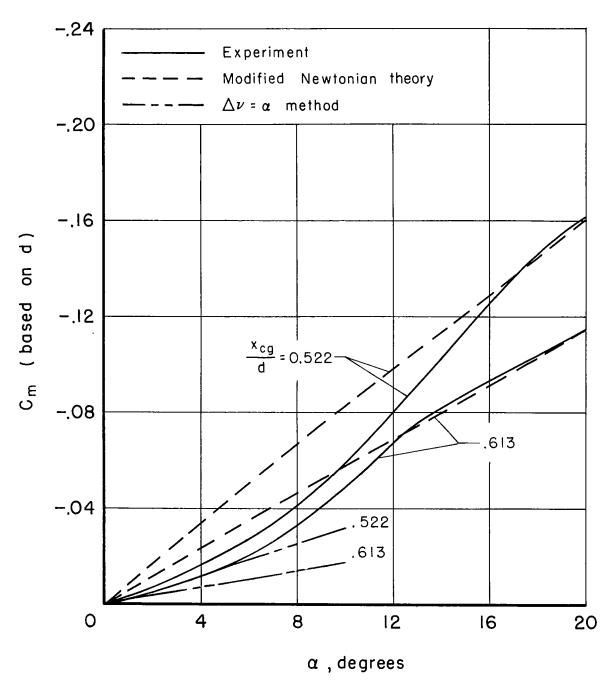
Figure 8.- Stability data of sphere-cone configuration at $M = 17$.
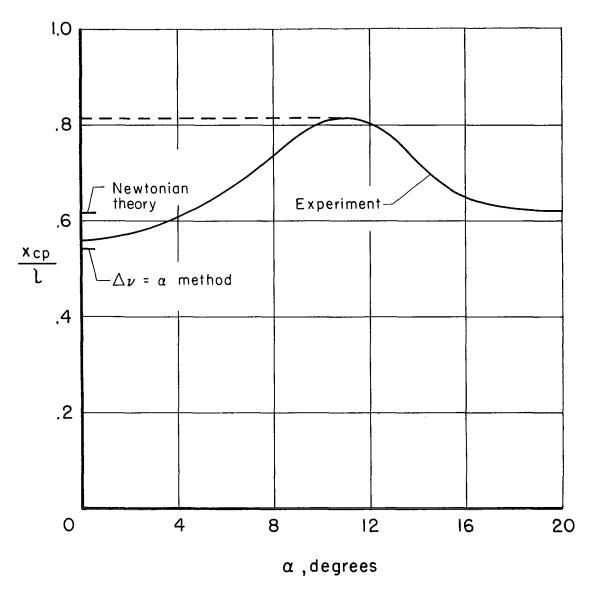
(b) Comparison of experimental and theoretical pitching-moment coefficients.
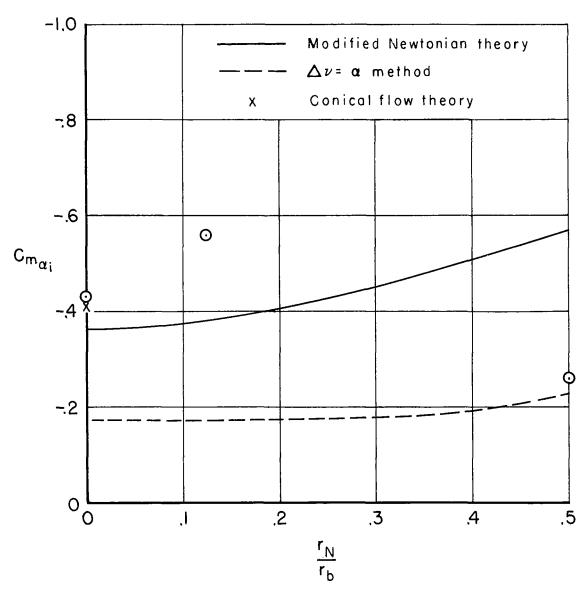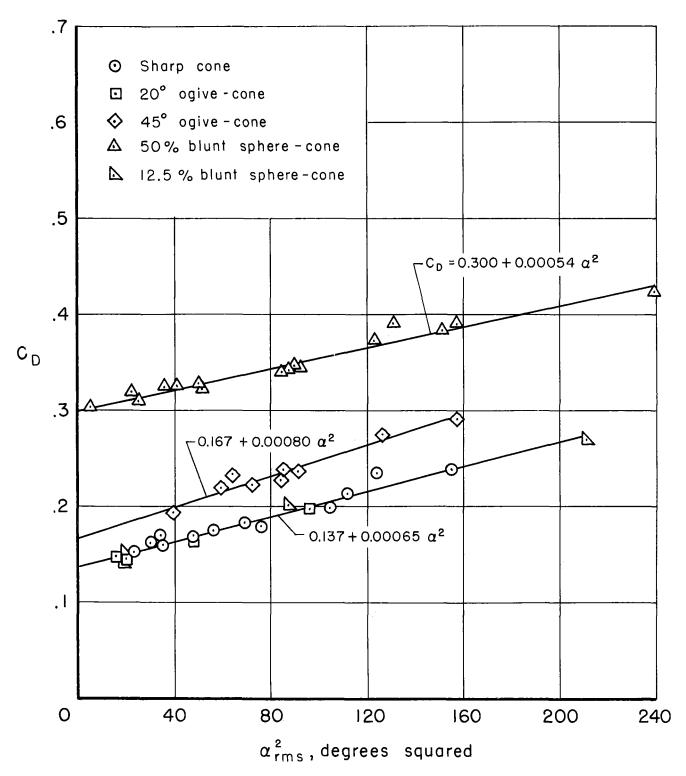
Figure 8.- Continued.

(c) Variation of center-of-pressure location with α.

Figure 8.- Concluded.
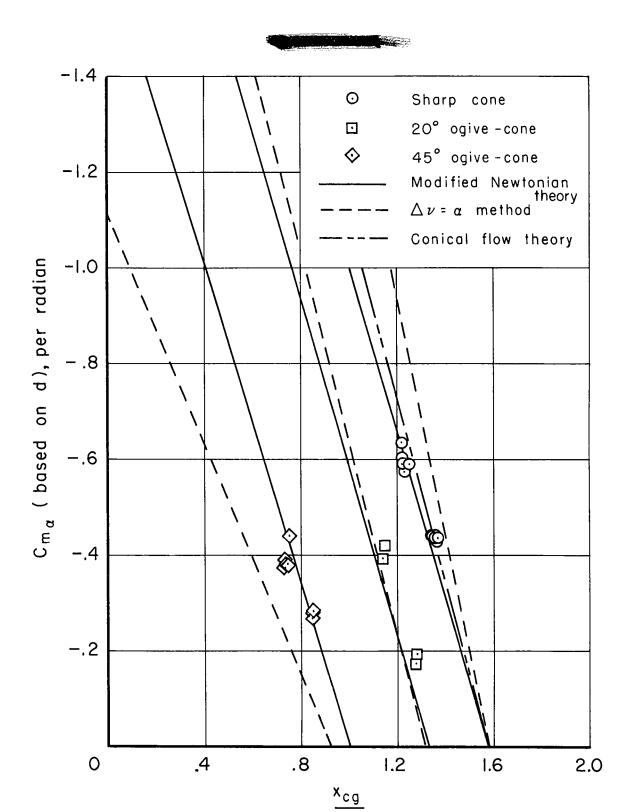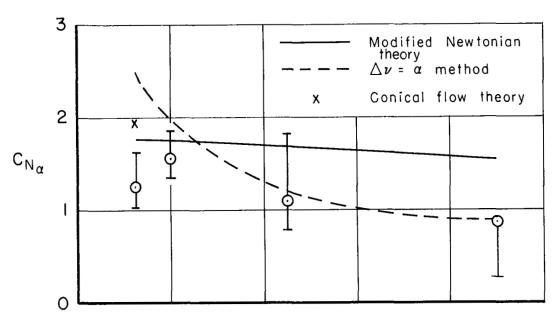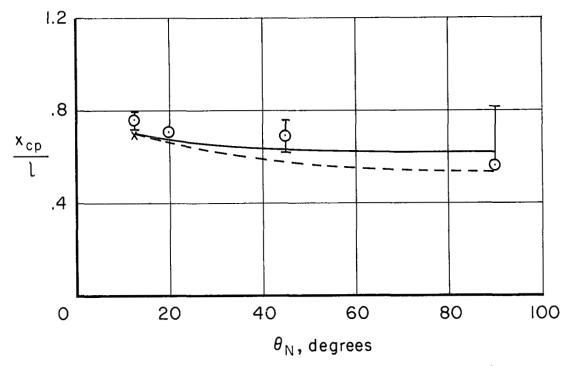
Figure 9.- Stability data of sharp-cone and ogive-cone configurations at M = 17.
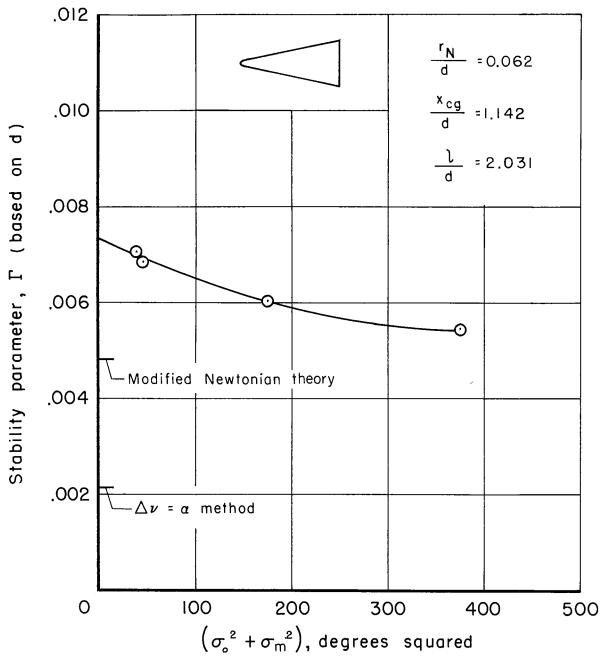
(a) Variation of normal-force-curve slope with nose-tangent angle.

(b) Variation of center-of-pressure location with nose-tangent angle.

Figure 10.- Comparison of experimental and theoretical results of conical configurations at M = 17.
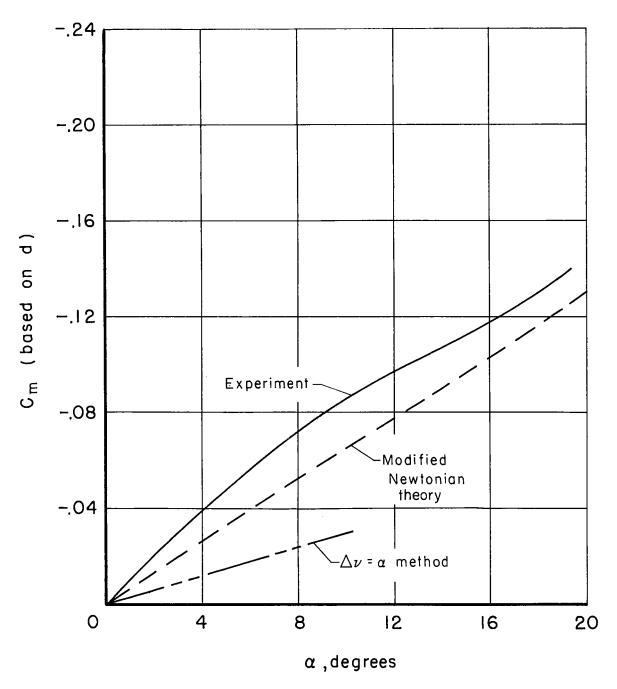
(a) Variation of stability parameter with $\left(\sigma_o^2 + \sigma_m^2\right)$.

Figure 11.- Stability data of 12.5-percent blunt sphere-cone at $M = 17$.

(b) Comparison of experimental and theoretical pitching-moment coefficients.
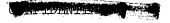
Figure 11.- Concluded.

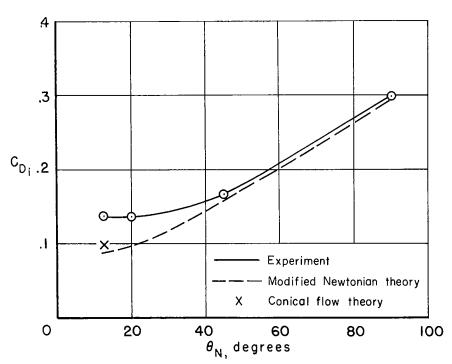Figure 12.- Effect of bluntness on stability of sphere-cone with $x_{cg}/d = 0.89$ from base.
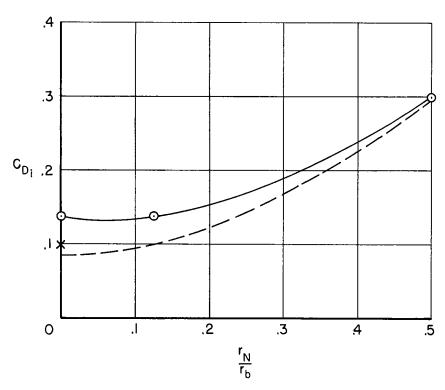
(a) Variation of drag with mean-squared angle of attack.

Figure 13.- Drag data of conical configurations at M = 17.

(b) Variation of initial (at $\alpha = 0$) drag coefficient with nose geometry.

(c) Effect of bluntness of sphere-cone on drag.

Figure 13.- Concluded.